Supplemental Materials for Multipartite Entanglement in Quantum Spin Liquids

Liuke Lyu,[1,2,3] Deeksha Chandorkar,[4,5] Samarth Kapoor,[4,5] So Takei,[4,5] Erik S. Sørensen,[6,*] and William Witczak-Krempa[1,2,3,†]

[1] *Département de Physique, Université de Montréal, Montréal, QC H3C 3J7, Canada*
[2] *Institut Courtois, Université de Montréal, Montréal (Québec), H2V 0B3, Canada*
[3] *Centre de Recherches Mathématiques, Université de Montréal, Montréal, QC, Canada, HC3 3J7*
[4] *Department of Physics, Queens College of the City University of New York, Queens, New York 11367, USA*
[5] *Physics Doctoral Program, Graduate Center of the City University of New York, New York, NY 10016, USA*
[6] *Department of Physics and Astronomy, McMaster University, Hamilton, Ontario L8S 4M1, Canada*

(Dated: June 23, 2025)

CONTENTS

I. GENUINE MULTIPARTITE NEGATIVITY AS A SEMIDEFINITE PROGRAM

Genuine Multipartite Negativity, as defined in Eq. (4), can be formulated as the following semidefinite program [1, 2]

$$\begin{aligned} \mathcal{N}(\rho) &= -\min \operatorname{tr}(\rho W) \\ \text{subject to } W &= P_m + Q_m^{T_m} \\ 0 &\leqslant P_m \\ 0 &\leqslant Q_m \leqslant I \text{ for all bipartitions } m \,|\, \bar{m} \end{aligned} \tag{1}$$

where W is an entanglement witness that is fully decomposable with respect to all bipartitions. For two operators A and B, the majorization $A \succeq B$ implies that $A - B$ is positive semidefinite. T_m refers to a partial transpose with respect to either part of the bipartition $m|\bar{m}$.

To compute the GMN, we use a modified version of the MATLAB package `pptmixer`[1], where the constraint $P_m \leqslant I$ is removed, as suggested in the later work [2] to provide a more physically transparent measure—specifically, a mixed convex roof of the minimum bipartite negativity. The semidefinite programs are modelled in MATLAB with the YALMIP toolbox [3] as parser, and solved using the MOSEK solver [4].

To motivate such an optimization, consider first a bipartite system. The negativity can be formulated as a semidefinite program

$$\begin{aligned} N(\rho) &= -\min \operatorname{tr}(\rho W) \\ \text{subject to } W &= Q^{T_1}, \\ 0 &\leq Q \leq I. \end{aligned} \tag{2}$$

Thus, the negativity is associated with an optimal PPT entanglement witness $W = Q^{T_1}$. Expanding the witness space to fully decomposable witnesses of the form

$$W' = P + Q^{T_1}, \tag{3}$$

with $P \geq 0$, does not enhance the detection capability in the bipartite case. In fact, if P is positive definite, the witness $W = Q^{T_1}$ is strictly finer than $W = P + Q^{T_1}$ [5]. However, in the multipartite case, the objective is to identify a witness that simultaneously detects entanglement across all bipartitions. In this setting, the optimal witness tailored for each bipartition may be suboptimal when a global criterion is required. Therefore, the use of fully decomposable witnesses becomes essential for quantifying genuine multipartite entanglement.

From the perspective of biseparable states, every biseparable state can be expressed as a convex combination of states that are separable with respect to the three bipartitions:

$$\rho^{\text{bs}} = p_1\, \rho^{\text{sep}}_{A|BC} + p_2\, \rho^{\text{sep}}_{B|AC} + p_3\, \rho^{\text{sep}}_{C|AB}, \tag{4}$$

with $p_1 + p_2 + p_3 = 1$ and $p_i \geq 0$. In contrast, the

GMN semidefinite program detects states lying outside the larger set

$$\rho^{\text{pmix}} = p_1\,\rho^{\text{PPT}}_{A|BC} + p_2\,\rho^{\text{PPT}}_{B|AC} + p_3\,\rho^{\text{PPT}}_{C|AB}, \tag{5}$$

where each component $\rho^{\text{PPT}}_{X|YZ}$ is PPT with respect to the corresponding bipartition.

II. ADDITIONAL ANALYSIS FOR THE KITAEV HONEYCOMB MODEL

A. Effective Hamiltonian for the small field Kitaev Spin Liquid

For the Kitaev model under a [111] field (main text equation 1), a perturbation expansion around $h = 0$ produces a 3-spin interaction which breaks time-reversal symmetry. The effective Hamiltonian at small field is

$$H_{\text{eff}} = \sum_{\langle i,j\rangle_\gamma} K_\gamma S_i^\gamma S_j^\gamma - \kappa \sum_{\langle\langle i,j,k\rangle\rangle} S_i^x S_j^y S_k^z, \tag{6}$$

where $\langle\langle i,j,k\rangle\rangle$ denotes ordered neighbouring sites and $\kappa = 3^{-2/3}h^3$. The chiral term stabilizes a gapped topological phase with non-Abelian anyons [6]. This model can be solved exactly in the Majorana fermion representation [7], and a computation of the hexagonal plaquette RDM can be found in section III.

B. Evolution of the MMES in the Kitaev model.

To visualize the evolution of GME with frustration, Fig. S1 plots the tripartite GMN of the hexagonal plaquette and all its nested subregions for the Kitaev model in a [111] field. Frustration is maximum at $h = 0$, and decreases with the field. The minimal multipartite-entangled subregion (MMES) changes in a stepwise fashion: at zero field the MMES is the full hexagon; it remains so up to $h \approx 0.50$ in the intermediate phase, then shrinks to the five-spin cluster (hexagon minus one site); near $h = h_{c2} \approx 0.64$ the four-spin cluster takes over; and beyond $h \approx 0.70$ the MMES reduces to the three adjacent spins of the high-field paramagnet. This hierarchy corroborates the MMES picture introduced in the main text.

C. Certifying Separability with Adaptive Polytope Algorithm

Table S1 summarizes our separability analysis for key reduced density matrices. For each subregion we bracket the critical value of the tuning parameter—field h in the Kitaev model or chirality λ in the Kagome model—between a lower bound obtained with the adaptive-polytope algorithm [8] and an upper bound extracted either from GMN (for biseparability) or the PPT criterion (for full separability). Whenever the interval $[\text{LB}, \text{UB}]$ lies entirely below the parameter range of interest, the state is rigorously certified biseparable; when it lies entirely above, GME is confirmed. In several cases (e.g. the three-spin ring around a hexagon) the bounds overlap, leaving a narrow, inconclusive window, but the qualitative picture is unambiguous: small, non-loopy clusters are biseparable throughout broad parameter ranges, whereas GME appears only when the cluster contains a closed loop.

Because the biseparable set is convex and of full measure, a state that lies strictly inside it remains biseparable under any sufficiently small perturbation—be it a change of coupling, a weak thermal admixture, or coupling to an environment. The intervals reported in Table S1 therefore demonstrate that the loopy-only pattern of GME identified in the main text is robust: non-loopy subregions remain GME-free across finite ranges of field or interaction, while loops retain finite GMN over the same ranges. In other words, the "entanglement frustration" that confines multipartite correlations to loops is not a fine-tuned artifact but a stable feature of these quantum spin liquids.

State	Parameter	LB (Polytope)	UB (GMN)
Kitaev $\rho_{3\text{–hex}}$	h_{s}	0.346	0.433
	h_{bs}	0.675	0.693
Kitaev $\rho_{4\text{–hex}}$	h_{bs}	0.632	0.641
Kitaev $\rho_{5\text{–hex}}$	h_{bs}	0.468	0.520
Kitaev $\rho_{6\text{–fork}}$	h_{bs}	0.130	0.147
Kagome $\rho_{3\text{–triangle}}$	λ_{bs}	0.250	0.300

TABLE S1. **Bounds on separability thresholds obtained from the adaptive–polytope method.** For each type of reduced density matrices, we list a lower bound (LB) and an upper bound (UB) on the critical value of the tuning parameter at which the state changes from separable to entangled: subscripts h_{s} (or λ_{s}) refer to *full separability*, while h_{bs} (or λ_{bs}) refer to *biseparability*. LB is obtained with the adaptive polytope algorithm of Ref. [8]; UB is set either by the genuine multipartite negativity (for biseparability) or by the PPT criterion (for full separability), using the data in Figs. 3, S1, and 6. "3-hex", "4-hex", and "5-hex" denote three, four, and five consecutive spins around a hexagonal plaquette; "6-fork" is the six-spin fork subregion; "3-triangle" is the triangular three-spin cluster on the Kagome lattice. For example, $\rho_{3\text{-hex}}$ is certified fully separable for $h \le 0.346$ and confirmed entangled for $h \ge 0.433$; the interval in between remains inconclusive.

D. GMN for N=24 Nauru Lattice

To further support the conclusions presented in the main text, we compute the GMN for the Kitaev Hon-

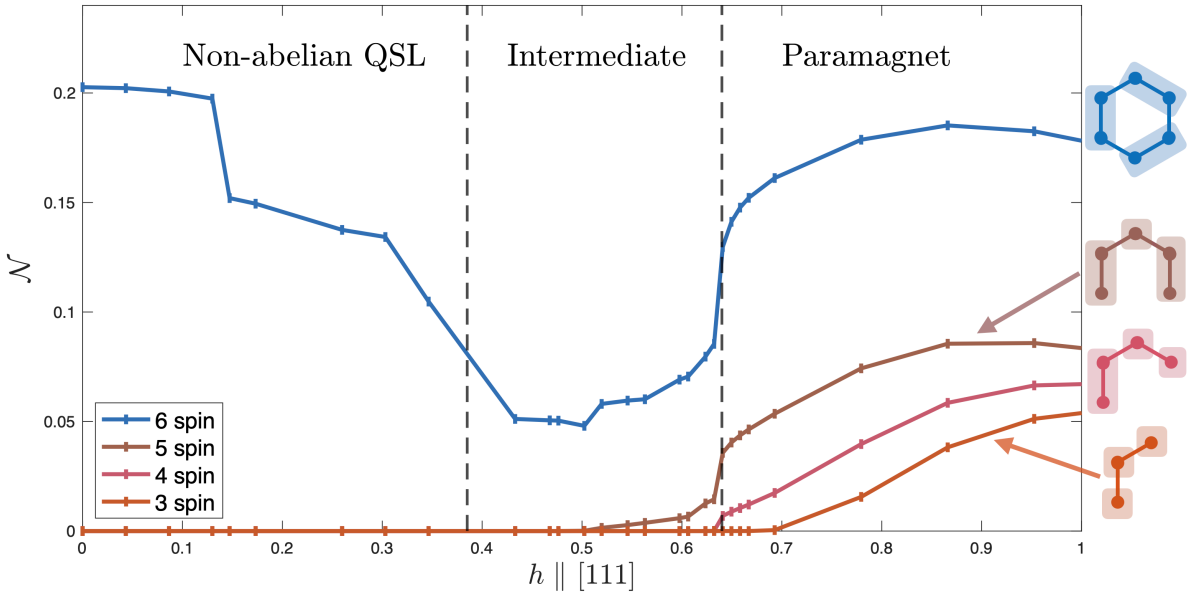

FIG. S1. **Evolution of the MMES in the Kitaev model.** Tripartite GMN $\mathcal{N}_3$ is shown for the hexagonal plaquette (blue) and its nested five-, four-, and three-spin subregions (shades of red) as a function of the [111] field h on the $N = 32$ cluster. Vertical dashed lines mark the non-Abelian QSL ($h < h_{c1}$), intermediate ($h_{c1} < h < h_{c2}$), and paramagnetic ($h > h_{c2}$) regimes. As frustration decreases with increasing field, the minimal multipartite-entangled subregion (MMES) shrinks in discrete steps: hexagon → five-spin → four-spin → three-spin, illustrating the hierarchy discussed in the main text.

eycomb Model on a smaller system, the $N = 24$ Nauru graph, and compare it with the results from the $N = 32$ Dyck graph. Figure S2 presents GMN as a function of the [111] magnetic field strength h, with the same structure as Fig. 3 in the main text.

The results for $N = 24$ largely mirror those for $N = 32$, confirming that GMN follows the same qualitative trends across system sizes. In the small-field regime, GMN is present in the hexagonal plaquette but absent in non-loopy or smaller subregions. Upon entering the intermediate phase, six-party GMN drops to zero, while GMN in the fork subregion begins to increase. In the paramagnetic phase, GMN grows across multiple subregions, regardless of their size or loop structure. The main difference observed in the $N = 24$ case is the presence of small oscillations in $\mathcal{N}_3$ and $\mathcal{N}_6$ between $h = 0.5$ and $h = 0.6$, which are absent in the $N = 32$ system. These oscillations likely stem from finite-size effects inherent to the smaller lattice geometry, rather than fundamental differences in the entanglement structure.

Overall, the consistency between the $N = 24$ and $N = 32$ results reinforces the validity of our conclusions regarding the role of loop-like multipartite entanglement in the Kitaev Honeycomb Model.

E. Minimum Negativity vs. [111] Field

To assess whether the distinctive "loopy" structure observed in our GMN analysis is already captured by bipartite measures, we compare the behaviour of the minimum negativity $N^{\min}$ with that of GMN. Since GMN is defined as a mixed convex roof extension of $N^{\min}$, we have $\mathcal{N}(\rho) \leq N^{min}(\rho)$ for any mixed state ρ. Figure S3 shows the tripartite and six-partite minimum negativity, $N_3^{\min}$ and $N_6^{\min}$, as functions of the magnetic field h.

In contrast to the GMN results in Fig. 3, which clearly differentiate between loopy (plaquette) and non-loopy (fork) subregions, the values of $N^{\min}$ do not exhibit such a distinction. Notably, in the small-field Kitaev spin liquid phase, $N^{\min}$ remains finite for the fork subregion even though the corresponding GMN vanishes. This observation demonstrates that the "loopy" entanglement structure is an intrinsically multipartite feature that cannot be captured by bipartite measures alone. Consequently, GMN is essential for revealing the collective entanglement properties inherent in quantum spin liquids.

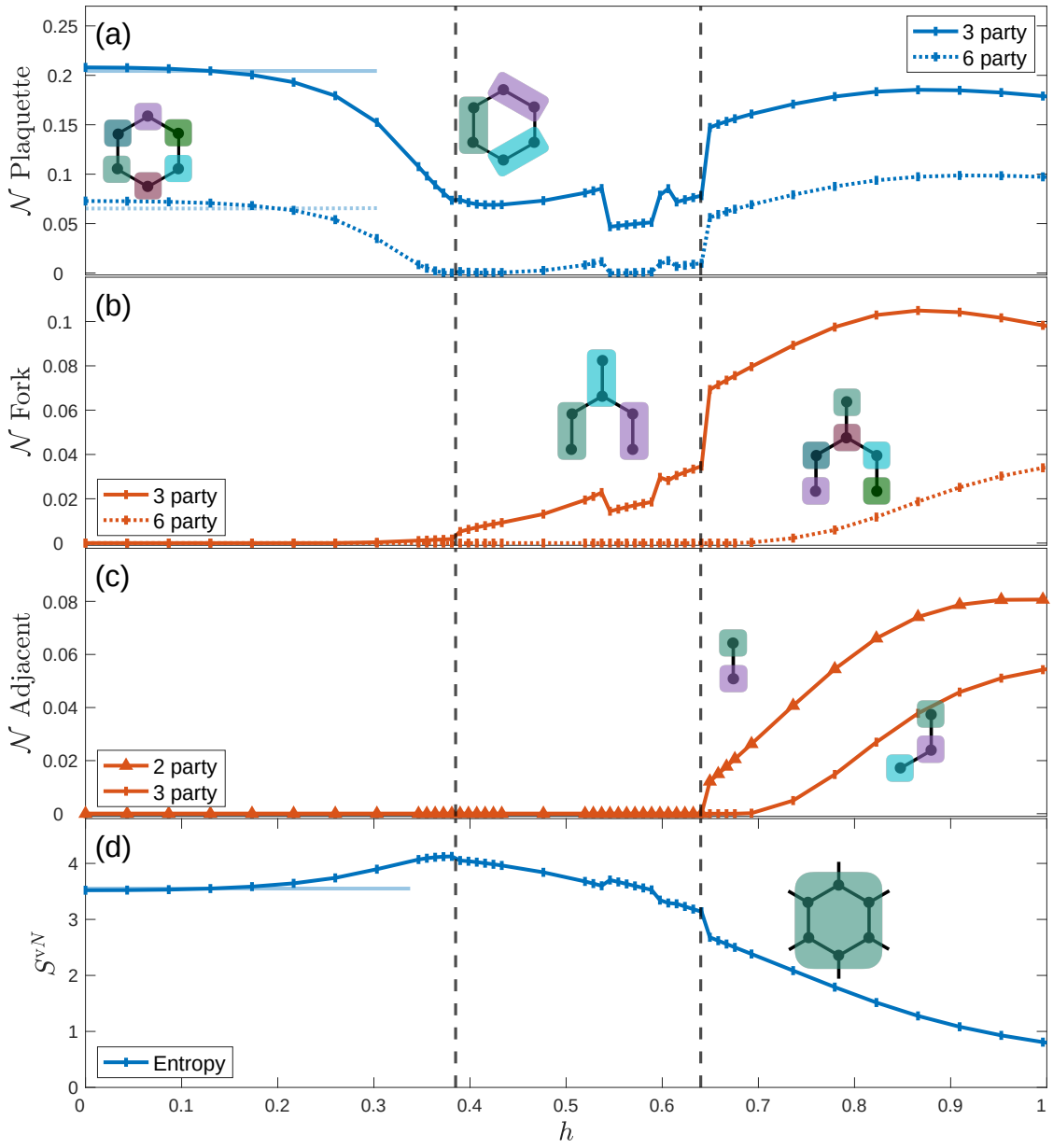

FIG. S2. **GMN vs h for the Kitaev Honeycomb Model on the $N = 24$ Nauru cluster.** Panels mirror those in Fig. 3: (a) tripartite ($\mathcal{N}_3$, solid) and six-partite ($\mathcal{N}_6$, dashed) GMN of the hexagon, (b) the same quantities for the fork subregion, and (c) bipartite ($\mathcal{N}_2$) and tripartite GMN for two- and three-spin clusters. Panel (d) adds the von Neumann entropy of the hexagon. The overall behaviour reproduces the $N = 32$ results: loop-confined GME at low field, the shift of the MMES from the hexagon to the three-spin cluster as the field increases, and phase boundaries at $h_{c1} = 0.38$ and $h_{c2} = 0.64$ (dashed lines). A minor difference is the appearance of small oscillations in (a) and (b) between $h = 0.50$ and 0.60, attributable to finite-size effects specific to the Nauru graph.

III. EXACT PLAQUETTE RDM OF KITAEV MODEL FROM MAJORANA FERMION METHODS

A. Model

The Kitaev honeycomb model is an exactly solvable model and a representative of quantum spin liquids with Majorana fermions coupled to emergent Z_2 gauge fields [7]. For ease of computation, we adopt a slightly different sign convention for $\hat{H}$ than in the main text; the Hamiltonian reads

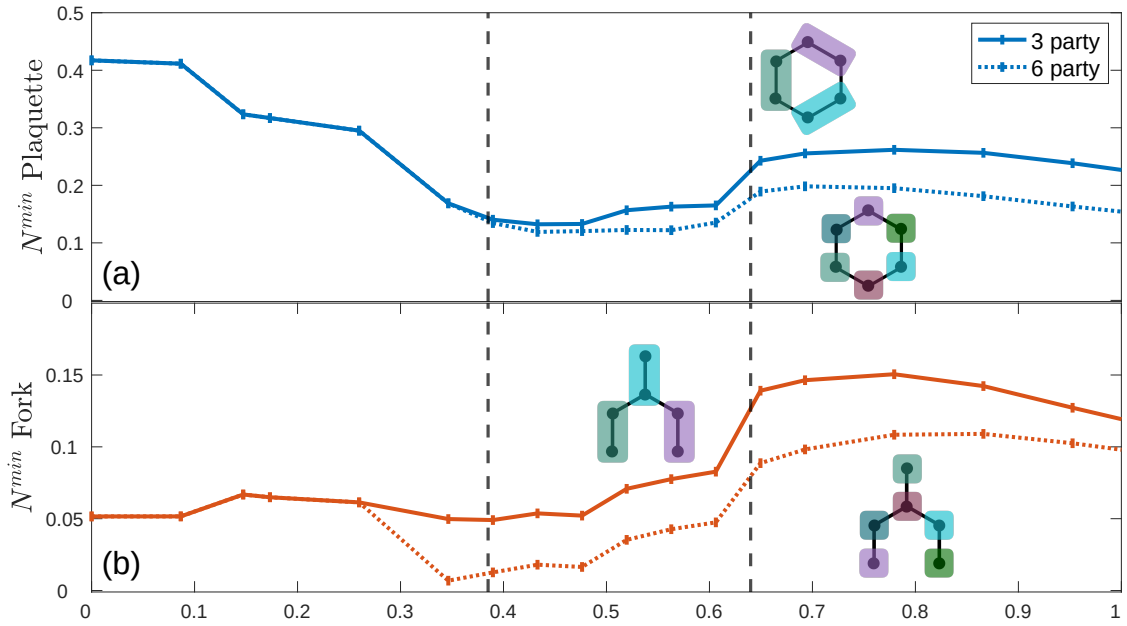

FIG. S3. **Minimum Negativity vs. [111] Field for the Kitaev Honeycomb Model.** Panel (a) shows the tripartite ($N_3^{\min}$) and six-partite ($N_6^{\min}$) minimum negativity for the hexagonal plaquette subregion as functions of the magnetic field h. Panel (b) presents the corresponding data for the fork subregion. Here, $N^{\min}$ is obtained by minimizing the bipartite negativity over all bipartitions into 3 or 6 parties. Notably, the minimum negativity does not clearly differentiate between the fork and plaquette subregions, in contrast to the genuine multipartite entanglement measures shown in Figure 3 of the main text, which capture the distinct "loopy" characteristics.

$$\hat{H} = -\sum_{\{\alpha=x,y,z\}} \sum_{\langle ij \rangle} J^{\alpha} \hat{\sigma}_i^{\alpha} \hat{\sigma}_j^{\alpha} , \tag{7}$$

where spin-1/2 moments on the honeycomb lattice – represented as Pauli operators – interact only through nearest neighbour Ising exchange J^{α} between sites i and j on sublattices A and B, respectively; here, $\alpha = x, y, z$ labels the different nearest neighbour bond directions, as shown in Fig. S4.

Equation (7) can be solved exactly via fermionization of the Pauli operators. This can be seen by first writing the spin on each site n as a composite of two Majorana fermion operators: $\hat{\sigma}_n^{\alpha} \equiv i\hat{\gamma}_n^{\alpha}\hat{\eta}_n$, where $\hat{\eta}_n$ are typically referred to as the matter fermions and $\hat{\gamma}_n^{\alpha}$ are identified as the bond fermions. These operators satisfy the canonical Majorana anticommutation relations: they square to one, and those of different types or on different sites anticommute. Defining the bond operators as $\hat{u}_{ij}^{\alpha} \equiv i\hat{\gamma}_i^{\alpha}\hat{\gamma}_j^{\alpha}$, Eq. (7) becomes quadratic in the matter fermions,

$$\hat{H} = i \sum_{\{\alpha=x,y,z\}} \sum_{\langle ij \rangle} J^{\alpha} \hat{u}_{ij}^{\alpha} \hat{\eta}_i \hat{\eta}_j . \tag{8}$$

The fermionic Hilbert space introduced via the fermionization procedure above has extra states that are related by a gauge transformation. The condition $-i\hat{\sigma}_n^x\hat{\sigma}_n^y\hat{\sigma}_n^z = 1$, which follows from the properties of the Pauli matrices, is not necessarily true in the extended Hilbert space. One may therefore define the operator

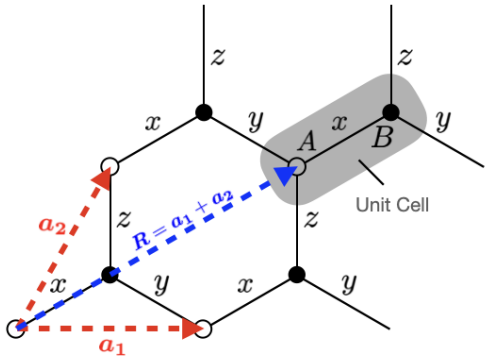

FIG. S4. A 2×2 honeycomb lattice with sublattices A and B. The A sites form a triangular lattice with primitive vectors $\boldsymbol{a_1}$ and $\boldsymbol{a_2}$. Each unit cell (denoted by $\boldsymbol{R}$) contains one spin from both sublattices joined by an x-link. A reference unit cell is illustrated in the figure.

$\hat{D}_n \equiv -i\hat{\sigma}_n^x\hat{\sigma}_n^y\hat{\sigma}_n^z = \hat{\gamma}_n^x\hat{\gamma}_n^y\hat{\gamma}_n^z\hat{\eta}_n$, and fix the gauge with the condition, $\hat{D}_n|\Psi\rangle = |\Psi\rangle$. Any state $|\Psi\rangle$ in the extended space can then be projected into the physical space using the projector

$$\hat{P} = \bigotimes_{\forall n \in A,B} \frac{1 + \hat{D}_n}{2} . \tag{9}$$

B. Ground State

The flux operator $\hat{W}_p = \hat{\sigma}_1^x\hat{\sigma}_2^y\hat{\sigma}_3^z\hat{\sigma}_4^x\hat{\sigma}_5^y\hat{\sigma}_6^z$, for any plaquette p on the honeycomb lattice (see Fig. S5), is conserved. Here, the spins $1,\ldots,6$ are labelled for each plaquette according to the convention in Fig. S5. These operators can be expressed solely in terms of the bond operators $\hat{u}_{ij}^\alpha$. Since these bond operators commute with the Hamiltonian (8) and square to one, a gauge configuration $\hat{u}_{ij}^\alpha = \pm 1$ consistent with a given set of values $W_p \in \{\pm 1\}$ may be found.

In the thermodynamic limit, the flux of the ground state is zero [9]. For Z_2 gauge fields, this implies that the plaquette operators $\hat{W}_p$ are one for all p, and therefore, one can also set the bond operators to $\hat{u}_{ij}^\alpha = 1$. The resultant system is translationally invariant, rendering it suitable to Fourier methods.

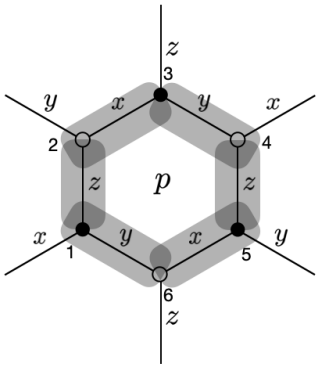

FIG. S5. A plaquette p of the honeycomb lattice

This procedure becomes more involved for the finite lattice, where the ground state is not necessarily flux-free [10], and may not be gauge-equivalent to the configuration $\hat{u}_{ij}^\alpha = 1$. Therefore, one should pick a bond configuration $\hat{u}_{ij}^\alpha$, determine the ground state of the matter fermions $\hat{\eta}_n$ in (8), and then iterate over all the independent gauge configurations.

C. Fermion Ground State

Keeping the focus on thermodynamic systems, $\hat{u}_{ij}^\alpha$ is set to one to find the spectrum in the flux free sector. Introducing a complex fermion $\hat{f}_{\boldsymbol{R}} = (\hat{\eta}_{\boldsymbol{R},A} + i\hat{\eta}_{\boldsymbol{R},B})/2$ for each unit cell $\boldsymbol{R}$ (see Fig. S4), the Hamiltonian (8) may be rewritten as

$$\hat{H} = \sum_{\boldsymbol{k}} \begin{pmatrix} \hat{f}_{\boldsymbol{k}}^\dagger & \hat{f}_{-\boldsymbol{k}} \end{pmatrix} \begin{pmatrix} \xi_{\boldsymbol{k}} & i\Delta_{\boldsymbol{k}} \\ -i\Delta_{\boldsymbol{k}} & -\xi_{\boldsymbol{k}} \end{pmatrix} \begin{pmatrix} \hat{f}_{\boldsymbol{k}} \\ \hat{f}_{-\boldsymbol{k}}^\dagger \end{pmatrix}, \tag{10}$$

where $\xi_{\boldsymbol{k}} = \Re\{S_{\boldsymbol{k}}\}$, $\Delta_{\boldsymbol{k}} = \Im\{S_{\boldsymbol{k}}\}$ and $S_{\boldsymbol{k}} = J^x + J^y e^{i\boldsymbol{k}\cdot\boldsymbol{a}_1} + J^z e^{i\boldsymbol{k}\cdot\boldsymbol{a}_2}$. Here, $\boldsymbol{a}_1$ and $\boldsymbol{a}_2$ are the two primitive vectors of the triangular lattice formed by the unit cells, and $\boldsymbol{k}$ labels the wave vectors within the first Brillouin zone of the triangular lattice. The values of $\boldsymbol{k}$ depend on the boundary conditions.

Equation (10) can be diagonalized using a Bogoliubov transformation, $\hat{f}_{\boldsymbol{k}} = \cos\theta_{\boldsymbol{k}}\hat{a}_{\boldsymbol{k}} - i\sin\theta_{\boldsymbol{k}}\hat{a}_{-\boldsymbol{k}}^\dagger$, where

$$\cos\theta_{\boldsymbol{k}} = \sqrt{\frac{E_{\boldsymbol{k}} + \xi_{\boldsymbol{k}}}{2E_{\boldsymbol{k}}}}, \quad \sin\theta_{\boldsymbol{k}} = \mathrm{sgn}(\Delta_{\boldsymbol{k}})\sqrt{\frac{E_{\boldsymbol{k}} - \xi_{\boldsymbol{k}}}{2E_{\boldsymbol{k}}}}, \tag{11}$$

and $E_{\boldsymbol{k}} = \sqrt{\xi_{\boldsymbol{k}}^2 + \Delta_{\boldsymbol{k}}^2}$. All two-point correlation functions of the matter Majorana fermions can now be evaluated in the ground state and are given by

$$\begin{aligned} \langle \hat{\eta}_{A\boldsymbol{R}}\hat{\eta}_{B\boldsymbol{R}'}\rangle &= \frac{i}{N}\sum_{\boldsymbol{k}} \frac{\xi_{\boldsymbol{k}} - i\Delta_{\boldsymbol{k}}}{E_{\boldsymbol{k}}} e^{i\boldsymbol{k}\cdot(\boldsymbol{R}-\boldsymbol{R}')} \\ \langle \hat{\eta}_{A\boldsymbol{R}}\hat{\eta}_{A\boldsymbol{R}'}\rangle &= \langle \hat{\eta}_{B\boldsymbol{R}}\hat{\eta}_{B\boldsymbol{R}'}\rangle = \delta_{\boldsymbol{R}\boldsymbol{R}'}, \end{aligned} \tag{12}$$

where N is the total number of unit cells on the lattice.

D. Reduced Density Matrix

A general method to construct the reduced density matrix for the Kitaev model is presented in Ref. 11. Here, we follow a different approach that may be most useful when computing the reduced density matrix for small subregions containing a few spins. The six-spin reduced density matrix on a plaquette may be expressed generally as

$$\hat{\rho}_6 = \frac{1}{2^6}\sum_{\{\mu_i=0,x,y,z\}} \langle \hat{\sigma}_1^{\mu_1}\hat{\sigma}_2^{\mu_2}\ldots\hat{\sigma}_6^{\mu_6}\rangle_0 \, \hat{\sigma}_1^{\mu_1}\hat{\sigma}_2^{\mu_2}\ldots\hat{\sigma}_6^{\mu_6}, \tag{13}$$

where $\langle\hat{O}\rangle_0$ represents the expectation value of $\hat{O}$ in the ground state, $\{\hat{\sigma}_n^x, \hat{\sigma}_n^y, \hat{\sigma}_n^z\}$ is the vector of Pauli matrices on site n and $\hat{\sigma}^0$ is the 2×2 identity matrix. The task is then to find all the non-zero spin expectation values to construct the density matrix. In this subsection, the results are calculated for $J^x = J^y = J^z = -1$.

Since the flux operators $\hat{W}_p$ are conserved, the correlation function for any operator that does not conserve the flux must be zero. This renders all one-spin correlation functions zero, i.e., $\langle\hat{\sigma}_n^\mu\rangle = 0$. In the absence of a magnetic field, all correlation functions with odd number of spins are zero by time-reversal symmetry. The only non-zero two-spin correlation functions are those that are joined by a bond with spin components matching the bond type, e.g., $\langle\hat{\sigma}_1^z\hat{\sigma}_2^z\rangle$. Table S2 lists all non-zero two-spin correlations functions on a plaquette and their values in the thermodynamic limit.

Figure S6 shows the groupings corresponding to non-zero four-spin correlation functions on a plaquette. Each grouping can give rise to more than one non-zero correlation function, and these are all listed in Table S3. As shown in the third column, each correlation function can

be re-expressed solely in terms of the matter Majorana fermion operators after setting the bond operators $\hat{u}_{ij}^{\alpha}$ to one [12]. Using Wick's theorem and the two-point correlation functions Eq. (12), these correlation functions can then be evaluated, and their numerical values in the thermodynamic limit are presented in the fourth column.

Similarly, all non-zero six-spin correlation functions, their corresponding matter Majorana fermion representation, and their numerical values in the thermodynamic limit are presented in Table S4.

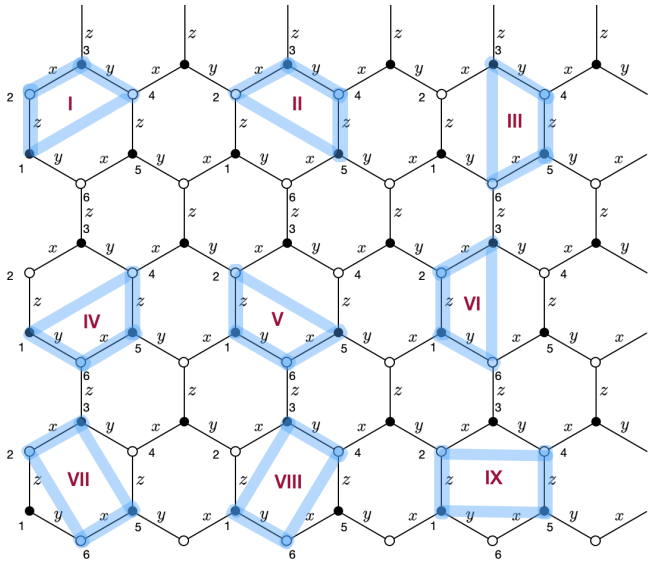

FIG. S6. Site groupings contributing to four-spin correlation functions.

TABLE S2. Two point functions for $J^x = J^y = J^z = -1$

Correlation function	Matter fermion representation	Expectation value
$\langle \hat{\sigma}_1^z \hat{\sigma}_2^z \rangle$	$+i \langle \hat{\eta}_1 \hat{\eta}_2 \rangle$	−0.5249
$\langle \hat{\sigma}_2^x \hat{\sigma}_3^x \rangle$	$-i \langle \hat{\eta}_2 \hat{\eta}_3 \rangle$	−0.5249
$\langle \hat{\sigma}_3^y \hat{\sigma}_4^y \rangle$	$+i \langle \hat{\eta}_3 \hat{\eta}_4 \rangle$	−0.5249
$\langle \hat{\sigma}_4^z \hat{\sigma}_5^z \rangle$	$-i \langle \hat{\eta}_4 \hat{\eta}_5 \rangle$	−0.5249
$\langle \hat{\sigma}_5^x \hat{\sigma}_6^x \rangle$	$+i \langle \hat{\eta}_5 \hat{\eta}_6 \rangle$	−0.5249
$\langle \hat{\sigma}_1^y \hat{\sigma}_6^y \rangle$	$+i \langle \hat{\eta}_1 \hat{\eta}_6 \rangle$	−0.5249

TABLE S3. Four point functions for each grouping in Figure S6 and $J^x = J^y = J^z = -1$

Group	Correlation function	Matter fermion representation	Expectation value
I	$\langle \hat{\sigma}_1^z \hat{\sigma}_2^y \hat{\sigma}_3^z \hat{\sigma}_4^y \rangle$	$-i \langle \hat{\eta}_1 \hat{\eta}_4 \rangle$	−0.1858
	$\langle \hat{\sigma}_1^z \hat{\sigma}_2^z \hat{\sigma}_3^y \hat{\sigma}_4^y \rangle$	$-\langle \hat{\eta}_1 \hat{\eta}_2 \hat{\eta}_3 \hat{\eta}_4 \rangle$	+0.3730
II	$\langle \hat{\sigma}_2^x \hat{\sigma}_3^z \hat{\sigma}_4^x \hat{\sigma}_5^z \rangle$	$+i \langle \hat{\eta}_2 \hat{\eta}_5 \rangle$	−0.1858
	$\langle \hat{\sigma}_2^x \hat{\sigma}_3^x \hat{\sigma}_4^z \hat{\sigma}_5^z \rangle$	$-\langle \hat{\eta}_2 \hat{\eta}_3 \hat{\eta}_4 \hat{\eta}_5 \rangle$	+0.3730
III	$\langle \hat{\sigma}_3^y \hat{\sigma}_4^x \hat{\sigma}_5^y \hat{\sigma}_6^x \rangle$	$-i \langle \hat{\eta}_3 \hat{\eta}_6 \rangle$	−0.1858
	$\langle \hat{\sigma}_3^y \hat{\sigma}_4^y \hat{\sigma}_5^x \hat{\sigma}_6^x \rangle$	$-\langle \hat{\eta}_3 \hat{\eta}_4 \hat{\eta}_5 \hat{\eta}_6 \rangle$	+0.3730
IV	$\langle \hat{\sigma}_1^y \hat{\sigma}_4^z \hat{\sigma}_5^y \hat{\sigma}_6^z \rangle$	$-i \langle \hat{\eta}_1 \hat{\eta}_4 \rangle$	−0.1858
	$\langle \hat{\sigma}_1^y \hat{\sigma}_4^z \hat{\sigma}_5^z \hat{\sigma}_6^y \rangle$	$+\langle \hat{\eta}_1 \hat{\eta}_4 \hat{\eta}_5 \hat{\eta}_6 \rangle$	+0.3730
V	$\langle \hat{\sigma}_1^x \hat{\sigma}_2^z \hat{\sigma}_5^x \hat{\sigma}_6^z \rangle$	$+i \langle \hat{\eta}_2 \hat{\eta}_5 \rangle$	−0.1858
	$\langle \hat{\sigma}_1^z \hat{\sigma}_2^z \hat{\sigma}_5^x \hat{\sigma}_6^x \rangle$	$-\langle \hat{\eta}_1 \hat{\eta}_2 \hat{\eta}_5 \hat{\eta}_6 \rangle$	+0.3730
VI	$\langle \hat{\sigma}_1^x \hat{\sigma}_2^y \hat{\sigma}_3^x \hat{\sigma}_6^y \rangle$	$-i \langle \hat{\eta}_3 \hat{\eta}_6 \rangle$	−0.1858
	$\langle \hat{\sigma}_1^y \hat{\sigma}_2^x \hat{\sigma}_3^x \hat{\sigma}_6^y \rangle$	$+\langle \hat{\eta}_1 \hat{\eta}_2 \hat{\eta}_3 \hat{\eta}_6 \rangle$	+0.3730
VII	$\langle \hat{\sigma}_2^x \hat{\sigma}_3^x \hat{\sigma}_5^x \hat{\sigma}_6^x \rangle$	$+\langle \hat{\eta}_2 \hat{\eta}_3 \hat{\eta}_5 \hat{\eta}_6 \rangle$	+0.2410
VIII	$\langle \hat{\sigma}_1^y \hat{\sigma}_3^y \hat{\sigma}_4^y \hat{\sigma}_6^y \rangle$	$-\langle \hat{\eta}_1 \hat{\eta}_3 \hat{\eta}_4 \hat{\eta}_6 \rangle$	+0.2410
IX	$\langle \hat{\sigma}_1^z \hat{\sigma}_2^z \hat{\sigma}_4^z \hat{\sigma}_5^z \rangle$	$+\langle \hat{\eta}_1 \hat{\eta}_2 \hat{\eta}_4 \hat{\eta}_5 \rangle$	+0.2410

TABLE S4. Six point functions for $J^x = J^y = J^z = -1$

Correlation function	Matter fermion representation	Expectation value
$\langle \hat{\sigma}_1^y \hat{\sigma}_2^x \hat{\sigma}_3^z \hat{\sigma}_4^x \hat{\sigma}_5^y \hat{\sigma}_6^z \rangle$	$+i \langle \hat{\eta}_1 \hat{\eta}_2 \rangle$	−0.5249
$\langle \hat{\sigma}_1^x \hat{\sigma}_2^z \hat{\sigma}_3^y \hat{\sigma}_4^x \hat{\sigma}_5^y \hat{\sigma}_6^z \rangle$	$-i \langle \hat{\eta}_2 \hat{\eta}_3 \rangle$	−0.5249
$\langle \hat{\sigma}_1^x \hat{\sigma}_2^y \hat{\sigma}_3^x \hat{\sigma}_4^z \hat{\sigma}_5^y \hat{\sigma}_6^z \rangle$	$+i \langle \hat{\eta}_3 \hat{\eta}_4 \rangle$	−0.5249
$\langle \hat{\sigma}_1^x \hat{\sigma}_2^y \hat{\sigma}_3^z \hat{\sigma}_4^y \hat{\sigma}_5^x \hat{\sigma}_6^z \rangle$	$-i \langle \hat{\eta}_4 \hat{\eta}_5 \rangle$	−0.5249
$\langle \hat{\sigma}_1^x \hat{\sigma}_2^y \hat{\sigma}_3^z \hat{\sigma}_4^x \hat{\sigma}_5^z \hat{\sigma}_6^y \rangle$	$+i \langle \hat{\eta}_5 \hat{\eta}_6 \rangle$	−0.5249
$\langle \hat{\sigma}_1^z \hat{\sigma}_2^y \hat{\sigma}_3^z \hat{\sigma}_4^x \hat{\sigma}_5^y \hat{\sigma}_6^x \rangle$	$+i \langle \hat{\eta}_1 \hat{\eta}_6 \rangle$	−0.5249
$\langle \hat{\sigma}_1^y \hat{\sigma}_2^x \hat{\sigma}_3^x \hat{\sigma}_4^z \hat{\sigma}_5^y \hat{\sigma}_6^z \rangle$	$-\langle \hat{\eta}_1 \hat{\eta}_2 \hat{\eta}_3 \hat{\eta}_4 \rangle$	+0.3730
$\langle \hat{\sigma}_1^x \hat{\sigma}_2^z \hat{\sigma}_3^y \hat{\sigma}_4^y \hat{\sigma}_5^x \hat{\sigma}_6^z \rangle$	$-\langle \hat{\eta}_2 \hat{\eta}_3 \hat{\eta}_4 \hat{\eta}_5 \rangle$	+0.3730
$\langle \hat{\sigma}_1^x \hat{\sigma}_2^y \hat{\sigma}_3^x \hat{\sigma}_4^z \hat{\sigma}_5^z \hat{\sigma}_6^y \rangle$	$-\langle \hat{\eta}_3 \hat{\eta}_4 \hat{\eta}_5 \hat{\eta}_6 \rangle$	+0.3730
$\langle \hat{\sigma}_1^z \hat{\sigma}_2^y \hat{\sigma}_3^z \hat{\sigma}_4^y \hat{\sigma}_5^x \hat{\sigma}_6^x \rangle$	$+\langle \hat{\eta}_1 \hat{\eta}_4 \hat{\eta}_5 \hat{\eta}_6 \rangle$	+0.3730
$\langle \hat{\sigma}_1^y \hat{\sigma}_2^x \hat{\sigma}_3^z \hat{\sigma}_4^z \hat{\sigma}_5^y \hat{\sigma}_6^x \rangle$	$-\langle \hat{\eta}_1 \hat{\eta}_2 \hat{\eta}_5 \hat{\eta}_6 \rangle$	+0.3730
$\langle \hat{\sigma}_1^z \hat{\sigma}_2^z \hat{\sigma}_3^y \hat{\sigma}_4^x \hat{\sigma}_5^x \hat{\sigma}_6^y \rangle$	$+\langle \hat{\eta}_1 \hat{\eta}_3 \hat{\eta}_4 \hat{\eta}_6 \rangle$	+0.3730
$\langle \hat{\sigma}_1^x \hat{\sigma}_2^z \hat{\sigma}_3^y \hat{\sigma}_4^z \hat{\sigma}_5^z \hat{\sigma}_6^y \rangle$	$+\langle \hat{\eta}_2 \hat{\eta}_3 \hat{\eta}_5 \hat{\eta}_6 \rangle$	+0.2410
$\langle \hat{\sigma}_1^z \hat{\sigma}_2^y \hat{\sigma}_3^z \hat{\sigma}_4^z \hat{\sigma}_5^y \hat{\sigma}_6^x \rangle$	$-\langle \hat{\eta}_1 \hat{\eta}_3 \hat{\eta}_4 \hat{\eta}_6 \rangle$	+0.2410
$\langle \hat{\sigma}_1^y \hat{\sigma}_2^x \hat{\sigma}_3^z \hat{\sigma}_4^y \hat{\sigma}_5^z \hat{\sigma}_6^x \rangle$	$+\langle \hat{\eta}_1 \hat{\eta}_2 \hat{\eta}_4 \hat{\eta}_5 \rangle$	+0.2410
$\langle \hat{\sigma}_1^z \hat{\sigma}_2^z \hat{\sigma}_3^y \hat{\sigma}_4^y \hat{\sigma}_5^x \hat{\sigma}_6^x \rangle$	$-i \langle \hat{\eta}_1 \hat{\eta}_2 \hat{\eta}_3 \hat{\eta}_4 \hat{\eta}_5 \hat{\eta}_6 \rangle$	−0.4363
$\langle \hat{\sigma}_1^y \hat{\sigma}_2^x \hat{\sigma}_3^z \hat{\sigma}_4^x \hat{\sigma}_5^z \hat{\sigma}_6^y \rangle$	$-i \langle \hat{\eta}_1 \hat{\eta}_2 \hat{\eta}_3 \hat{\eta}_4 \hat{\eta}_5 \hat{\eta}_6 \rangle$	−0.4363
$\langle \hat{\sigma}_1^x \hat{\sigma}_2^y \hat{\sigma}_3^z \hat{\sigma}_4^x \hat{\sigma}_5^y \hat{\sigma}_6^z \rangle$	$+1$	+1

E. Under a [111] magnetic field

Now we consider the addition of a magnetic field term,

$$H_b = -\sum_i \sum_{\{\alpha=x,y,z\}} h_\alpha \hat{\sigma}_i^\alpha \,, \tag{14}$$

where h_α are the components of the field. In the case of a weak magnetic field, an effective Hamiltonian may be found in the subspace of the flux-free states using perturbation theory. [7] In the isotropic case ($J^x = J^y = J^z = J$), the additional magnetic field term can then be expressed as

$$H_b \approx -\kappa \sum_{\langle\langle jkl \rangle\rangle} \hat{\sigma}_j^x \hat{\sigma}_k^y \hat{\sigma}_l^z \,, \tag{15}$$

where $\kappa = h_x h_y h_z/J^2$ in this section, and $\langle\langle jkl \rangle\rangle$ represents the sum over all spin triples that conserve the flux operators $\hat{W}_p$, as listed in Fig. S7. [7]

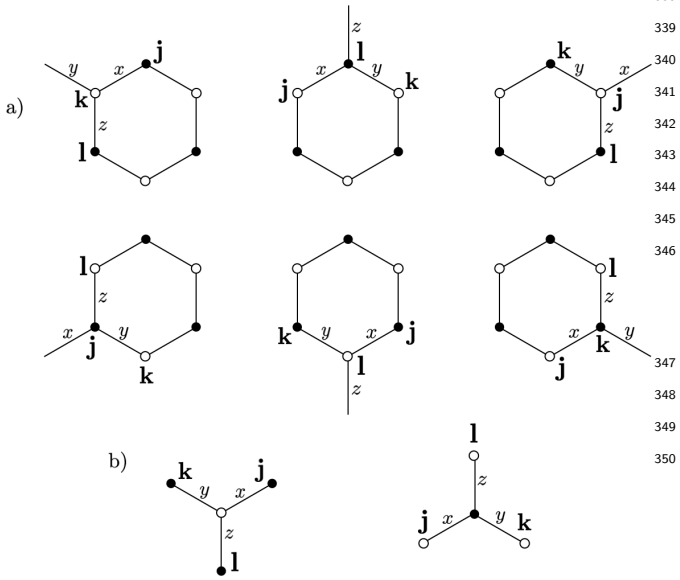

FIG. S7. Spin triple arrangements contributing to the projected Hamiltonian. (a) Spin triples on a plaquette. These correspond to operators quadratic in the matter fermions. (b) These configurations are associated with terms quartic in the matter fermions.

Fermionizing the spin operators as in Sec. III A, the Hamiltonian can be expressed as a sum of terms containing either two or four matter fermions. Following Ref. 7, we drop the four-fermion contributions in the weak magnetic field limit. Using the gauge choice $\hat{u}^{\alpha}_{ij} = 1$ and employing the same notation as Sec. III C, the Hamiltonian is given by,

$$\hat{H} = \sum_{\boldsymbol{k}} \begin{pmatrix} \hat{f}^{\dagger}_{\boldsymbol{k}} & \hat{f}_{-\boldsymbol{k}} \end{pmatrix} \begin{pmatrix} \xi_{\boldsymbol{k}} & i\Delta_{\boldsymbol{k}} + \delta_{\boldsymbol{k}} \\ -i\Delta_{\boldsymbol{k}} + \delta_{\boldsymbol{k}} & -\xi_{\boldsymbol{k}} \end{pmatrix} \begin{pmatrix} \hat{f}_{\boldsymbol{k}} \\ \hat{f}^{\dagger}_{-\boldsymbol{k}} \end{pmatrix}, \quad (16)$$

where $\delta_{\boldsymbol{k}} = -2\kappa[\sin \boldsymbol{k}\cdot\boldsymbol{a}_1 - \sin \boldsymbol{k}\cdot(\boldsymbol{a}_1 - \boldsymbol{a}_2) - \sin \boldsymbol{k}\cdot\boldsymbol{a}_2]$. This is diagonalized by the Boguliubov transformation, $\hat{f}_{\boldsymbol{k}} = \cos\theta_{\boldsymbol{k}}\hat{a}_{\boldsymbol{k}} - i\sin\theta_{\boldsymbol{k}}\hat{a}^{\dagger}_{-\boldsymbol{k}}$, where

$$\cos\theta_{\boldsymbol{k}} = \sqrt{\frac{E_{\boldsymbol{k}} + \xi_{\boldsymbol{k}}}{2E_{\boldsymbol{k}}}}, \quad \sin\theta_{\boldsymbol{k}} = \frac{\Delta_{\boldsymbol{k}} - i\delta_{\boldsymbol{k}}}{\sqrt{\Delta^2_{\boldsymbol{k}} + \delta^2_{\boldsymbol{k}}}}\sqrt{\frac{E_{\boldsymbol{k}} - \xi_{\boldsymbol{k}}}{2E_{\boldsymbol{k}}}}, \quad (17)$$

and $E_{\boldsymbol{k}} = \sqrt{\xi^2_{\boldsymbol{k}} + \Delta^2_{\boldsymbol{k}} + \delta^2_{\boldsymbol{k}}}$. The two-point correlation functions for the matter fermions can then be found,

$$\begin{aligned} \langle \hat{\eta}_{A\boldsymbol{R}}\hat{\eta}_{B\boldsymbol{R}'} \rangle &= \frac{i}{N}\sum_{\boldsymbol{k}} \frac{\xi_{\boldsymbol{k}} - i\Delta_{\boldsymbol{k}}}{E_{\boldsymbol{k}}} e^{i\boldsymbol{k}\cdot(\boldsymbol{R}-\boldsymbol{R}')} \\ \langle \hat{\eta}_{A\boldsymbol{R}}\hat{\eta}_{A\boldsymbol{R}'} \rangle &= \delta_{\boldsymbol{R}\boldsymbol{R}'} + \frac{1}{N}\sum_{\boldsymbol{k}} \frac{\delta_{\boldsymbol{k}}}{E_{\boldsymbol{k}}} e^{i\boldsymbol{k}\cdot(\boldsymbol{R}-\boldsymbol{R}')} \\ \langle \hat{\eta}_{B\boldsymbol{R}}\hat{\eta}_{B\boldsymbol{R}'} \rangle &= \delta_{\boldsymbol{R}\boldsymbol{R}'} - \frac{1}{N}\sum_{\boldsymbol{k}} \frac{\delta_{\boldsymbol{k}}}{E_{\boldsymbol{k}}} e^{i\boldsymbol{k}\cdot(\boldsymbol{R}-\boldsymbol{R}')}. \end{aligned} \quad (18)$$

The reduced density matrix for the plaquette can be calculated in terms of spin correlation functions using Eq. (13). While the flux-conserving two-spin, four-spin, and six-spin operators contribute to the sum in Eq. (13) at zero field, the breaking of time-reversal symmetry allows the inclusion of operators involving an odd number of spins, provided that they conserve flux. In particular, the one-spin contribution to the reduced density matrix remains absent. The three-spin correlation functions are nonzero for the operators listed in Fig. S7, and Table S6 lists all nonzero three-spin correlations functions on a plaquette and their values in the thermodynamic limit.

The list of all nonzero spin correlation functions, their corresponding matter Majorana fermion representations and their numerical values for $J = -1$ and $\kappa = 0.1$ are presented in Tables S5, S6, S7, S8 and S9.

TABLE S5. Nonzero two point functions for $J^x = J^y = J^z = -1$ and $\kappa = 0.1$

Correlation function	Matter fermion representation	Expectation value
$\langle \hat{\sigma}^z_1\hat{\sigma}^z_2 \rangle$	$+i\langle \hat{\eta}_1\hat{\eta}_2 \rangle$	−0.5152
$\langle \hat{\sigma}^x_2\hat{\sigma}^x_3 \rangle$	$-i\langle \hat{\eta}_2\hat{\eta}_3 \rangle$	−0.5152
$\langle \hat{\sigma}^y_3\hat{\sigma}^y_4 \rangle$	$+i\langle \hat{\eta}_3\hat{\eta}_4 \rangle$	−0.5152
$\langle \hat{\sigma}^z_4\hat{\sigma}^z_5 \rangle$	$-i\langle \hat{\eta}_4\hat{\eta}_5 \rangle$	−0.5152
$\langle \hat{\sigma}^x_5\hat{\sigma}^x_6 \rangle$	$+i\langle \hat{\eta}_5\hat{\eta}_6 \rangle$	−0.5152
$\langle \hat{\sigma}^y_1\hat{\sigma}^y_6 \rangle$	$+i\langle \hat{\eta}_1\hat{\eta}_6 \rangle$	−0.5152

TABLE S6. Non-zero three point functions for $J^x = J^y = J^z = -1$ and $\kappa = 0.1$

Correlation function	Matter fermion representation	Expectation value
$\langle \hat{\sigma}^z_1\hat{\sigma}^y_2\hat{\sigma}^x_3 \rangle$	$-i\langle \hat{\eta}_1\hat{\eta}_3 \rangle$	+0.1119
$\langle \hat{\sigma}^x_2\hat{\sigma}^z_3\hat{\sigma}^y_4 \rangle$	$-i\langle \hat{\eta}_2\hat{\eta}_4 \rangle$	+0.1119
$\langle \hat{\sigma}^y_3\hat{\sigma}^x_4\hat{\sigma}^z_5 \rangle$	$-i\langle \hat{\eta}_3\hat{\eta}_5 \rangle$	+0.1119
$\langle \hat{\sigma}^z_4\hat{\sigma}^y_5\hat{\sigma}^x_6 \rangle$	$-i\langle \hat{\eta}_4\hat{\eta}_6 \rangle$	+0.1119
$\langle \hat{\sigma}^y_1\hat{\sigma}^x_5\hat{\sigma}^z_6 \rangle$	$+i\langle \hat{\eta}_1\hat{\eta}_5 \rangle$	+0.1119
$\langle \hat{\sigma}^x_1\hat{\sigma}^z_2\hat{\sigma}^y_6 \rangle$	$+i\langle \hat{\eta}_2\hat{\eta}_6 \rangle$	+0.1119

TABLE S7. Non-zero four point functions for each grouping in Figure S6 and $J^x = J^y = J^z = -1$ and $\kappa = 0.1$

Group	Correlation function	Matter fermion representation	Expectation value
I	$\langle\hat{\sigma}_1^z\hat{\sigma}_2^y\hat{\sigma}_3^z\hat{\sigma}_4^y\rangle$	$-i\langle\hat{\eta}_1\hat{\eta}_4\rangle$	−0.1694
	$\langle\hat{\sigma}_1^z\hat{\sigma}_2^z\hat{\sigma}_3^y\hat{\sigma}_4^y\rangle$	$-\langle\hat{\eta}_1\hat{\eta}_2\hat{\eta}_3\hat{\eta}_4\rangle$	+0.3402
II	$\langle\hat{\sigma}_2^x\hat{\sigma}_3^z\hat{\sigma}_4^x\hat{\sigma}_5^z\rangle$	$+i\langle\hat{\eta}_2\hat{\eta}_5\rangle$	−0.1694
	$\langle\hat{\sigma}_2^x\hat{\sigma}_3^x\hat{\sigma}_4^z\hat{\sigma}_5^z\rangle$	$-\langle\hat{\eta}_2\hat{\eta}_3\hat{\eta}_4\hat{\eta}_5\rangle$	+0.3402
III	$\langle\hat{\sigma}_3^y\hat{\sigma}_4^x\hat{\sigma}_5^y\hat{\sigma}_6^x\rangle$	$-i\langle\hat{\eta}_3\hat{\eta}_6\rangle$	−0.1694
	$\langle\hat{\sigma}_3^y\hat{\sigma}_4^y\hat{\sigma}_5^x\hat{\sigma}_6^x\rangle$	$-\langle\hat{\eta}_3\hat{\eta}_4\hat{\eta}_5\hat{\eta}_6\rangle$	+0.3402
IV	$\langle\hat{\sigma}_1^y\hat{\sigma}_4^z\hat{\sigma}_5^y\hat{\sigma}_6^z\rangle$	$-i\langle\hat{\eta}_1\hat{\eta}_4\rangle$	−0.1694
	$\langle\hat{\sigma}_1^y\hat{\sigma}_4^z\hat{\sigma}_5^z\hat{\sigma}_6^y\rangle$	$+\langle\hat{\eta}_1\hat{\eta}_4\hat{\eta}_5\hat{\eta}_6\rangle$	+0.3402
V	$\langle\hat{\sigma}_1^x\hat{\sigma}_2^z\hat{\sigma}_5^x\hat{\sigma}_6^z\rangle$	$+i\langle\hat{\eta}_2\hat{\eta}_5\rangle$	−0.1694
	$\langle\hat{\sigma}_1^z\hat{\sigma}_2^z\hat{\sigma}_5^x\hat{\sigma}_6^x\rangle$	$-\langle\hat{\eta}_1\hat{\eta}_2\hat{\eta}_5\hat{\eta}_6\rangle$	+0.3402
VI	$\langle\hat{\sigma}_1^x\hat{\sigma}_2^y\hat{\sigma}_3^x\hat{\sigma}_6^y\rangle$	$-i\langle\hat{\eta}_3\hat{\eta}_6\rangle$	−0.1694
	$\langle\hat{\sigma}_1^y\hat{\sigma}_2^x\hat{\sigma}_3^x\hat{\sigma}_6^y\rangle$	$+\langle\hat{\eta}_1\hat{\eta}_2\hat{\eta}_3\hat{\eta}_6\rangle$	+0.3402
VII	$\langle\hat{\sigma}_2^x\hat{\sigma}_3^x\hat{\sigma}_5^x\hat{\sigma}_6^x\rangle$	$+\langle\hat{\eta}_2\hat{\eta}_3\hat{\eta}_5\hat{\eta}_6\rangle$	+0.2493
VIII	$\langle\hat{\sigma}_1^y\hat{\sigma}_3^y\hat{\sigma}_4^y\hat{\sigma}_6^y\rangle$	$-\langle\hat{\eta}_1\hat{\eta}_3\hat{\eta}_4\hat{\eta}_6\rangle$	+0.2493
IX	$\langle\hat{\sigma}_1^z\hat{\sigma}_2^z\hat{\sigma}_4^z\hat{\sigma}_5^z\rangle$	$+\langle\hat{\eta}_1\hat{\eta}_2\hat{\eta}_4\hat{\eta}_5\rangle$	+0.2493

TABLE S8. Non-zero five point functions for $J^x = J^y = J^z = -1$ and $\kappa = 0.1$

Correlation function	Matter fermion representation	Expectation value
$\langle\hat{\sigma}_1^y\hat{\sigma}_2^0\hat{\sigma}_3^y\hat{\sigma}_4^x\hat{\sigma}_5^y\hat{\sigma}_6^z\rangle$	$-i\langle\hat{\eta}_1\hat{\eta}_3\rangle$	+0.1119
$\langle\hat{\sigma}_1^y\hat{\sigma}_2^0\hat{\sigma}_3^y\hat{\sigma}_4^y\hat{\sigma}_5^x\hat{\sigma}_6^z\rangle$	$-\langle\hat{\eta}_1\hat{\eta}_3\hat{\eta}_4\hat{\eta}_5\rangle$	−0.0963
$\langle\hat{\sigma}_1^y\hat{\sigma}_2^0\hat{\sigma}_3^y\hat{\sigma}_4^x\hat{\sigma}_5^z\hat{\sigma}_6^y\rangle$	$+\langle\hat{\eta}_1\hat{\eta}_3\hat{\eta}_5\hat{\eta}_6\rangle$	−0.0963
$\langle\hat{\sigma}_1^x\hat{\sigma}_2^z\hat{\sigma}_3^0\hat{\sigma}_4^z\hat{\sigma}_5^y\hat{\sigma}_6^z\rangle$	$-i\langle\hat{\eta}_2\hat{\eta}_4\rangle$	+0.1119
$\langle\hat{\sigma}_1^x\hat{\sigma}_2^z\hat{\sigma}_3^0\hat{\sigma}_4^z\hat{\sigma}_5^z\hat{\sigma}_6^y\rangle$	$+\langle\hat{\eta}_2\hat{\eta}_4\hat{\eta}_5\hat{\eta}_6\rangle$	−0.0963
$\langle\hat{\sigma}_1^z\hat{\sigma}_2^z\hat{\sigma}_3^0\hat{\sigma}_4^z\hat{\sigma}_5^y\hat{\sigma}_6^x\rangle$	$+\langle\hat{\eta}_1\hat{\eta}_2\hat{\eta}_4\hat{\eta}_6\rangle$	−0.0963
$\langle\hat{\sigma}_1^x\hat{\sigma}_2^y\hat{\sigma}_3^x\hat{\sigma}_4^0\hat{\sigma}_5^x\hat{\sigma}_6^z\rangle$	$-i\langle\hat{\eta}_3\hat{\eta}_5\rangle$	+0.1119
$\langle\hat{\sigma}_1^y\hat{\sigma}_2^x\hat{\sigma}_3^x\hat{\sigma}_4^0\hat{\sigma}_5^x\hat{\sigma}_6^z\rangle$	$+\langle\hat{\eta}_1\hat{\eta}_2\hat{\eta}_3\hat{\eta}_5\rangle$	−0.0963
$\langle\hat{\sigma}_1^z\hat{\sigma}_2^y\hat{\sigma}_3^x\hat{\sigma}_4^0\hat{\sigma}_5^x\hat{\sigma}_6^x\rangle$	$+\langle\hat{\eta}_1\hat{\eta}_3\hat{\eta}_5\hat{\eta}_6\rangle$	−0.0963
$\langle\hat{\sigma}_1^x\hat{\sigma}_2^y\hat{\sigma}_3^z\hat{\sigma}_4^y\hat{\sigma}_5^0\hat{\sigma}_6^y\rangle$	$-i\langle\hat{\eta}_4\hat{\eta}_6\rangle$	+0.1119
$\langle\hat{\sigma}_1^x\hat{\sigma}_2^z\hat{\sigma}_3^y\hat{\sigma}_4^y\hat{\sigma}_5^0\hat{\sigma}_6^y\rangle$	$-\langle\hat{\eta}_2\hat{\eta}_3\hat{\eta}_4\hat{\eta}_6\rangle$	−0.0963
$\langle\hat{\sigma}_1^y\hat{\sigma}_2^x\hat{\sigma}_3^z\hat{\sigma}_4^y\hat{\sigma}_5^0\hat{\sigma}_6^y\rangle$	$+\langle\hat{\eta}_1\hat{\eta}_2\hat{\eta}_4\hat{\eta}_6\rangle$	−0.0963
$\langle\hat{\sigma}_1^z\hat{\sigma}_2^y\hat{\sigma}_3^z\hat{\sigma}_4^x\hat{\sigma}_5^z\hat{\sigma}_6^0\rangle$	$+i\langle\hat{\eta}_1\hat{\eta}_5\rangle$	+0.1119
$\langle\hat{\sigma}_1^z\hat{\sigma}_2^z\hat{\sigma}_3^y\hat{\sigma}_4^x\hat{\sigma}_5^z\hat{\sigma}_6^0\rangle$	$+\langle\hat{\eta}_1\hat{\eta}_2\hat{\eta}_3\hat{\eta}_5\rangle$	−0.0963
$\langle\hat{\sigma}_1^z\hat{\sigma}_2^y\hat{\sigma}_3^x\hat{\sigma}_4^z\hat{\sigma}_5^z\hat{\sigma}_6^0\rangle$	$-\langle\hat{\eta}_1\hat{\eta}_3\hat{\eta}_4\hat{\eta}_5\rangle$	−0.0963
$\langle\hat{\sigma}_1^0\hat{\sigma}_2^x\hat{\sigma}_3^z\hat{\sigma}_4^x\hat{\sigma}_5^y\hat{\sigma}_6^x\rangle$	$+i\langle\hat{\eta}_2\hat{\eta}_6\rangle$	+0.1119
$\langle\hat{\sigma}_1^0\hat{\sigma}_2^x\hat{\sigma}_3^z\hat{\sigma}_4^y\hat{\sigma}_5^x\hat{\sigma}_6^x\rangle$	$+\langle\hat{\eta}_2\hat{\eta}_4\hat{\eta}_5\hat{\eta}_6\rangle$	−0.0963
$\langle\hat{\sigma}_1^0\hat{\sigma}_2^x\hat{\sigma}_3^x\hat{\sigma}_4^z\hat{\sigma}_5^y\hat{\sigma}_6^x\rangle$	$-\langle\hat{\eta}_2\hat{\eta}_3\hat{\eta}_4\hat{\eta}_6\rangle$	−0.0963

TABLE S9. Non-zero six point functions for $J^x = J^y = J^z = -1$ and $\kappa = 0.1$

Correlation function	Matter fermion representation	Expectation value
$\langle\hat{\sigma}_1^y\hat{\sigma}_2^x\hat{\sigma}_3^z\hat{\sigma}_4^x\hat{\sigma}_5^y\hat{\sigma}_6^z\rangle$	$+i\langle\hat{\eta}_1\hat{\eta}_2\rangle$	−0.5152
$\langle\hat{\sigma}_1^x\hat{\sigma}_2^z\hat{\sigma}_3^y\hat{\sigma}_4^x\hat{\sigma}_5^y\hat{\sigma}_6^z\rangle$	$-i\langle\hat{\eta}_2\hat{\eta}_3\rangle$	−0.5152
$\langle\hat{\sigma}_1^x\hat{\sigma}_2^y\hat{\sigma}_3^z\hat{\sigma}_4^x\hat{\sigma}_5^y\hat{\sigma}_6^z\rangle$	$+i\langle\hat{\eta}_3\hat{\eta}_4\rangle$	−0.5152
$\langle\hat{\sigma}_1^x\hat{\sigma}_2^y\hat{\sigma}_3^z\hat{\sigma}_4^y\hat{\sigma}_5^x\hat{\sigma}_6^z\rangle$	$-i\langle\hat{\eta}_4\hat{\eta}_5\rangle$	−0.5152
$\langle\hat{\sigma}_1^x\hat{\sigma}_2^y\hat{\sigma}_3^z\hat{\sigma}_4^x\hat{\sigma}_5^z\hat{\sigma}_6^y\rangle$	$+i\langle\hat{\eta}_5\hat{\eta}_6\rangle$	−0.5152
$\langle\hat{\sigma}_1^z\hat{\sigma}_2^y\hat{\sigma}_3^z\hat{\sigma}_4^x\hat{\sigma}_5^y\hat{\sigma}_6^x\rangle$	$+i\langle\hat{\eta}_1\hat{\eta}_6\rangle$	−0.5152
$\langle\hat{\sigma}_1^y\hat{\sigma}_2^x\hat{\sigma}_3^x\hat{\sigma}_4^z\hat{\sigma}_5^y\hat{\sigma}_6^z\rangle$	$-\langle\hat{\eta}_1\hat{\eta}_2\hat{\eta}_3\hat{\eta}_4\rangle$	+0.3402
$\langle\hat{\sigma}_1^x\hat{\sigma}_2^z\hat{\sigma}_3^y\hat{\sigma}_4^y\hat{\sigma}_5^x\hat{\sigma}_6^z\rangle$	$-\langle\hat{\eta}_2\hat{\eta}_3\hat{\eta}_4\hat{\eta}_5\rangle$	+0.3402
$\langle\hat{\sigma}_1^x\hat{\sigma}_2^y\hat{\sigma}_3^x\hat{\sigma}_4^z\hat{\sigma}_5^z\hat{\sigma}_6^y\rangle$	$-\langle\hat{\eta}_3\hat{\eta}_4\hat{\eta}_5\hat{\eta}_6\rangle$	+0.3402
$\langle\hat{\sigma}_1^z\hat{\sigma}_2^y\hat{\sigma}_3^z\hat{\sigma}_4^y\hat{\sigma}_5^x\hat{\sigma}_6^x\rangle$	$+\langle\hat{\eta}_1\hat{\eta}_4\hat{\eta}_5\hat{\eta}_6\rangle$	+0.3402
$\langle\hat{\sigma}_1^y\hat{\sigma}_2^x\hat{\sigma}_3^z\hat{\sigma}_4^x\hat{\sigma}_5^z\hat{\sigma}_6^y\rangle$	$-\langle\hat{\eta}_1\hat{\eta}_2\hat{\eta}_5\hat{\eta}_6\rangle$	+0.3402
$\langle\hat{\sigma}_1^z\hat{\sigma}_2^z\hat{\sigma}_3^y\hat{\sigma}_4^x\hat{\sigma}_5^y\hat{\sigma}_6^x\rangle$	$+\langle\hat{\eta}_1\hat{\eta}_2\hat{\eta}_3\hat{\eta}_6\rangle$	+0.3402
$\langle\hat{\sigma}_1^x\hat{\sigma}_2^z\hat{\sigma}_3^y\hat{\sigma}_4^x\hat{\sigma}_5^z\hat{\sigma}_6^y\rangle$	$+\langle\hat{\eta}_2\hat{\eta}_3\hat{\eta}_5\hat{\eta}_6\rangle$	+0.2493
$\langle\hat{\sigma}_1^z\hat{\sigma}_2^y\hat{\sigma}_3^x\hat{\sigma}_4^z\hat{\sigma}_5^y\hat{\sigma}_6^x\rangle$	$-\langle\hat{\eta}_1\hat{\eta}_3\hat{\eta}_4\hat{\eta}_6\rangle$	+0.2493
$\langle\hat{\sigma}_1^y\hat{\sigma}_2^x\hat{\sigma}_3^z\hat{\sigma}_4^y\hat{\sigma}_5^x\hat{\sigma}_6^z\rangle$	$+\langle\hat{\eta}_1\hat{\eta}_2\hat{\eta}_4\hat{\eta}_5\rangle$	+0.2493
$\langle\hat{\sigma}_1^z\hat{\sigma}_2^z\hat{\sigma}_3^y\hat{\sigma}_4^y\hat{\sigma}_5^x\hat{\sigma}_6^x\rangle$	$-i\langle\hat{\eta}_1\hat{\eta}_2\hat{\eta}_3\hat{\eta}_4\hat{\eta}_5\hat{\eta}_6\rangle$	−0.3712
$\langle\hat{\sigma}_1^y\hat{\sigma}_2^x\hat{\sigma}_3^x\hat{\sigma}_4^z\hat{\sigma}_5^z\hat{\sigma}_6^y\rangle$	$-i\langle\hat{\eta}_1\hat{\eta}_2\hat{\eta}_3\hat{\eta}_4\hat{\eta}_5\hat{\eta}_6\rangle$	−0.3712
$\langle\hat{\sigma}_1^x\hat{\sigma}_2^y\hat{\sigma}_3^z\hat{\sigma}_4^x\hat{\sigma}_5^y\hat{\sigma}_6^z\rangle$	+1	+1

IV. FINITE SIZE ANALYSIS FOR THE KAGOMÉ HEISENBERG ANTIFERROMAGNETIC

To assess the robustness of our ED results in the thermodynamic limit, we consider the model at $J_2 = \lambda = 0$ and compute the tripartite GMN $\mathcal{N}_3$ for the Bowtie and Hexagon subregions across system sizes $N = 12, 18, 24$, and 36 (see Fig. S8). The values of $\mathcal{N}_3$ appear to have converged by $N = 36$, with the Bowtie subregion stabilizing at 0.0141 and the Hexagon subregion at 0. This suggests that the absence of GMN in the Hexagon and its persistence in the Bowtie are intrinsic properties of the Kagome Heisenberg Antiferromagnet rather than finite-size effects. These findings reinforce the distinction between loopy and non-loopy subregions in hosting multipartite entanglement.

V. MULTIPARTY ENTANGLEMENT IN TOPOLOGICAL STRING-NET MODELS

The string-net model proposed by Levin and Wen [13] describes a large class of topologically ordered states, including quantum spin liquids. It is defined on a honeycomb lattice with spin degrees of freedom residing on the edges (see Fig. S9). The Hamiltonian takes the form

$$H = -\sum_v Q_v - \sum_p B_p, \tag{19}$$

where Q_v is a vertex operator enforcing local constraints at each trivalent vertex, and B_p is a plaquette operator that measures the flux through a plaquette and provides

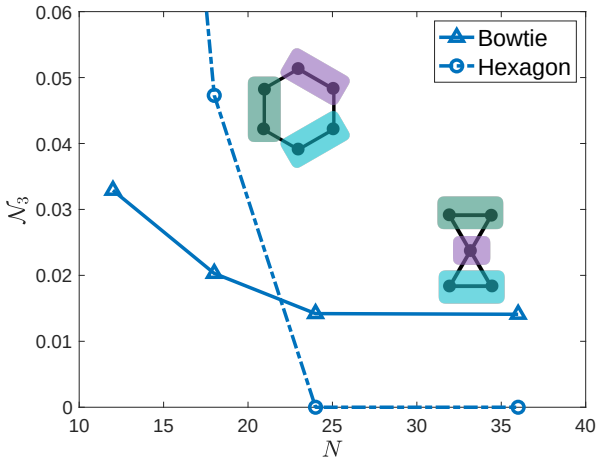

FIG. S8. **Finite-size scaling of GMN in the Kagome Heisenberg Model.** Tripartite GMN ($\mathcal{N}_3$) for the Bowtie and Hexagon subregions as a function of system size N, computed for the Kagome model with $J_2 = \lambda = 0$. Results are shown for $N = 12, 18, 24$, and 36. The values of $\mathcal{N}_3$ appear to have converged by $N = 36$, with the Bowtie subregion stabilizing at 0.0141 and the Hexagon subregion at 0. These results suggest that the thermodynamic limit is well-approximated by the largest system sizes considered.

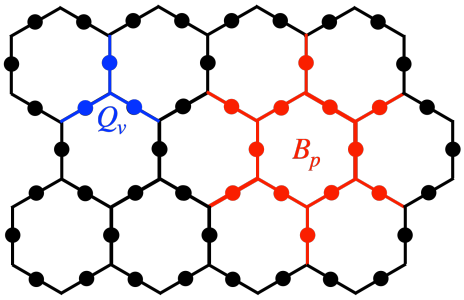

FIG. S9. **Hexagonal lattice for the string-net model.** The diagram illustrates the honeycomb lattice used in the string-net model of Levin and Wen [13], where spins reside on the edges. The vertex operator Q_v (a three-spin interaction) enforces local constraints at each trivalent vertex, while the plaquette operator B_p (a 12-spin interaction) measures the magnetic flux through each plaquette and drives the dynamics of the string-net configurations.

the dynamics of string-net configurations. The ground states of this model satisfy $\langle Q_v \rangle = \langle B_p \rangle = 1$, ensuring local gauge invariance. A key feature of the string-net construction is that its fixed-point ground state is *fully specified* by a pair of local tensors, namely the six-index tensor F^{ijm}_{kln} and the one-index tensor d_i. In particular, we can derive the branching rules from the F tensor, which provides a local gauge constraint for any three edges which share a vertex. Consider the subspace S of string configurations which satisfy all local constraints, the fixed-point wavefunction can be written as $|\Phi\rangle = \sum_{s\in S} a(s)\,|s\rangle$, and the matrix elements of the RDM of a subregion A can be written as

$$[\rho_A]_{s_A s_{A'}} = \sum_{s_B} a(s_A s_B) a^*(s_{A'} s_B) \tag{20}$$

where $(s_A, s_B), (s_{A'}, s_B) \in S$. If we cannot find any subregion s_B which is compatible with two distinct configurations s_A and $s_{A'}$, then all off-diagonal elements vanish and thus the RDM is fully separable. A similar argument was made for a general spin-1/2 system where the valid spin flips form a group [14], which can be applied to show that non-loopy subregions of the $\mathbb{Z}_2$ gauge theory are fully separable. We generalize this to arbitrary Abelian string-nets:

Reduced state ρ_A of any non-loopy subregion A is fully separable in Abelian string-nets.

To see this, notice that in an Abelian string-net, the branching rules at each vertex have no multiplicity: once two of the three incident edge labels are fixed, the third is determined uniquely. Now, if the region A is a tree (i.e. has no loops), then fixing a global configuration s_B on the complement immediately fixes the labels on the edges of A that touch B. From there, we can "peel" the tree inward: at each trivalent vertex in A, two of its edges have already been determined, so the third edge label follows uniquely from the branching rule. By iterating this process, we recover at most one valid s_A for each s_B. Hence, no two distinct s_A can coexist with the same s_B, all off-diagonal matrix elements $\rho_{s_A, s_{A'}}$ vanish, and ρ_A is fully separable.

For a general string-net, the reduced density matrix of a simply connected region A takes a diagonal form [15]

$$\rho_A = \sum_{\{q,m\}} p_{\{q,m\}} \,|\{q,m\}\rangle\langle\{q,m\}| \tag{21}$$

where $\{q, m\}$ labels the string configuration on the tree-like boundary of A. Each boundary configuration specifies a unique interior wavefunction $|\{q,m\}\rangle$ via successive F-moves, and its weight factorizes as $p_{\{q,m\}} = \prod_m d_{q_m}$, depending only on the external legs that link A to its complement. Using this expression, we evaluate ρ_A for the 12-site region that encloses a single hexagon—the support of the B_p operator (red area in Fig. S9). From this parent RDM, we can trace out selected spins to obtain smaller subregions and then compute their GMN, allowing a systematic study of multiparty entanglement at and below the hexagon scale. Because the Hilbert space dimension grows rapidly with the number of string types, exact GMN can be computed only for modest cluster sizes: up to six sites when the local dimension is $d = 2$, and up to four sites for $d = 3$. For some larger clusters, we instead determine rigorous lower bounds. Armed with these tools, we now survey GME across a range of Abelian and non-Abelian string-net models.

$\mathbb{Z}_2$ gauge theory and the Double Semion Model

The simplest case is an Abelian string-net with one string type of no branching rules, the model is specified by

$$\begin{aligned} d_0 &= 1, \quad d_1 = F_{110}^{110} = \pm 1, \\ F_{000}^{000} &= F_{101}^{101} = F_{011}^{011} = 1, \\ F_{111}^{000} &= F_{001}^{110} = F_{010}^{101} = F_{100}^{011} = 1, \end{aligned} \tag{22}$$

with all other elements of F vanishing. The corresponding fixed-point wave functions are given by

$$\Phi_{\pm}(X) = (\pm 1)^{X_c}, \tag{23}$$

where X_c is the number of disconnected closed string components in the configuration X. Φ_+ is associated with a Z_2 gauge theory, while Φ_- corresponds to a double semion model.

To investigate the local entanglement properties of these fixed-point wave functions $\Phi_\pm$, we study the RDMs for various local subregions. For subregions that do not enclose any loop, the RDM is diagonal, so the state is fully separable. For the hexagonal plaquette the RDM takes the form of an *X state*—a state whose only non-zero matrix elements lie on the diagonal and anti-diagonal. More precisely, an n-qubit X state is defined by

$$[X(a,c)]_{ij} = \begin{cases} a_i, & \text{if } i = j, \\ c_i, & \text{if } j = \bar{i}, \\ 0, & \text{otherwise}, \end{cases} \tag{24}$$

where $I_{[n]}$ is the set of all n-bit indices (e.g., $I_{[6]}$ for a hexagon), a_i and c_i are real numbers corresponding to the diagonal and anti-diagonal elements, and $\bar{i}$ denotes the bitwise complement of i.

In our case, the state ρ_+ corresponding to Φ_+ has uniform diagonal elements $a_i = 1/64$ and uniform anti-diagonal elements $c_i = 1/64$ for all $i \in I_{[6]}$. In contrast, while ρ_- has the same diagonal entries $a_i = 1/64$, its anti-diagonal elements c_i depend on the number of groups of consecutive 1's (under periodic boundary conditions): if the number of groups is even, then $c_i = -1/64$; if odd, $c_i = 1/64$. For instance, configurations like 000000, 000111, 001101, and 101010 (which correspond to 0, 1, 2, and 3 groups respectively) acquire the appropriate sign for c_i. Using Theorem 5.3 in [16], it can be shown that ρ_+ is fully separable. Although ρ_- is not fully separable, it has zero GMN along the tripartition (12)(34)(56) around the plaquette and can be further shown biseparable using the separability algorithm.

Fibonacci String-Net Model

The Fibonacci string-net is a non-abelian string-net with one type of string, specified by

$$\begin{aligned} d_0 &= 1, \quad d_1 = \gamma, \\ F_{110}^{110} &= \gamma^{-1}, \quad F_{111}^{110} = \gamma^{-1/2}, \\ F_{110}^{111} &= \gamma^{-1/2}, \quad F_{111}^{111} = -\gamma^{-1}. \end{aligned} \tag{25}$$

In the above, the nontrivial entries correspond to the case $i = j = k = l = 1$ when using the notation F_{kln}^{ijm}. The remaining elements of F are defined by

$$F_{kln}^{ijm} = \delta_{m,i,j}\, \delta_{m,k,l}\, \delta_{n,j,k}\, \delta_{n,i,l}, \tag{26}$$

where

$$\delta_{ijk} = \begin{cases} 1, & \text{if } \{i,j,k\} \text{ is allowed}, \\ 0, & \text{otherwise}. \end{cases} \tag{27}$$

All contiguous subregions up to six spins exhibit no detectable GME: every three- and four-site cluster has a diagonal reduced density matrix and is therefore fully separable (hence zero bipartite negativity and zero GMN), while five-site clusters are fully PPT along all bipartitions—and thus no GMN—and six-site clusters, although some contain bipartite negativity, still carry zero GMN. The hexagonal plaquette likewise has no GMN. However, we find a finite tripartite GMN for the 12-site region that encloses a single hexagon by evaluating a lower bound: $\mathcal{N}_3 \geq 0.0607$.

$\mathbb{Z}_3$ gauge theory

The next case is an Abelian model with two types of strings, 1 and 2 where $2 = 1^*$, so they correspond to two orientations of the string. The model is specified by the branching rules $\{\{1,1,1\},\{2,2,2\}\}$ and the F tensor

$$\begin{aligned} d_0 &= d_1 = d_2 = 1, \\ F_{kln}^{ijm} &= \delta_{m,i,j}\, \delta_{m,k,l}\, \delta_{n,j,k}\, \delta_{n,i,l}, \end{aligned} \tag{28}$$

and the fixed point wavefunction $\Phi(X) = 1$ for every configuration satisfying the branching rules.

All non-loopy subregions are diagonal and thus fully separable, as proved by the general result for Abelian string-nets. For the hexagonal plaquette, the RDM for the $\mathbb{Z}_3$ gauge theory is fully PPT, and thus has no GMN.

S_3 gauge theory

We now consider the first non-abelian string-net model, with two string types and branching rules $\{\{1,2,2\},\{2,2,2\}\}$. The strings are unoriented, so $1^* = 1, 2^* = 2$. The d and F tensors are

$$d_0 = d_1 = 1, \quad d_2 = 2 \tag{29}$$

$$F_{110}^{110} = F_{222}^{110} = F_{212}^{212} = 1 \tag{30}$$

$$F_{222}^{212} = -1 \tag{31}$$

and F_{22n}^{22m} is given by the matrix

$$F_{22n}^{22m} = \begin{pmatrix} \frac{1}{2} & \frac{1}{2} & \frac{1}{\sqrt{2}} \\ \frac{1}{2} & \frac{1}{2} & -\frac{1}{\sqrt{2}} \\ \frac{1}{\sqrt{2}} & -\frac{1}{\sqrt{2}} & 0 \end{pmatrix}. \tag{32}$$

All three- and four-spin clusters have diagonal reduced density matrices and are therefore fully separable

(hence zero bipartite negativity and zero GMN). Five-spin patches, although non-diagonal, remain fully PPT and thus exhibit neither bipartite negativity nor GMN. The six-spin hexagonal plaquette does display bipartite entanglement, but our lower-bound does not detect a finite GMN. Similarly, no GMN was detected for the 12-site subregion enclosing a hexagon.

Ising String-Net Model

Finally, we consider the Ising string-net model, a non-abelian model with local dimension 3 that accommodates two distinct string types. In this model, following Kitaev's notation (See Table.1 in Ref. [7]), we define

$$1 \text{ (vacuum)}, \quad \varepsilon \text{ (fermion)}, \quad \sigma \text{ (vortex)},$$

The quantum dimensions are $d_1 = d_\varepsilon = 1, d_\sigma = \sqrt{2}$, and the fusion rules are given by

$$\varepsilon \times \varepsilon = 1, \quad \varepsilon \times \sigma = \sigma, \quad \sigma \times \sigma = 1 + \varepsilon.$$

The nontrivial elements of the F tensor are specified as follows:

$$\begin{aligned} F^{\sigma\sigma 1}_{\sigma\sigma 1} &= \frac{1}{\sqrt{2}}, \quad F^{\sigma\sigma 1}_{\sigma\sigma\varepsilon} = \frac{1}{\sqrt{2}}, \\ F^{\sigma\sigma\varepsilon}_{\sigma\sigma 1} &= \frac{1}{\sqrt{2}}, \quad F^{\sigma\sigma\varepsilon}_{\sigma\sigma\varepsilon} = -\frac{1}{\sqrt{2}}, \\ F^{\varepsilon\sigma\sigma}_{\varepsilon\sigma\sigma} &= -1, \quad F^{\sigma\varepsilon\sigma}_{\sigma\varepsilon\sigma} = -1. \end{aligned} \tag{33}$$

In all other cases, the F tensor elements are determined by Eq. (26), analogous to the Fibonacci string-net model.

All three- and four-site clusters have diagonal reduced density matrices and are therefore fully separable (zero bipartite negativity and zero GMN). Five-site clusters, though non-diagonal, remain fully PPT and thus likewise exhibit neither bipartite negativity nor GMN. In contrast, the 6-site hexagonal plaquette retains genuine tripartite entanglement: our lower-bound calculation yields $\mathcal{N}_3 \geq 0.0112$.

* sorensen@mcmaster.ca

† w.witczak-krempa@umontreal.ca

[1] B. Jungnitsch, T. Moroder, and O. Gühne, Taming Multiparticle Entanglement, Physical Review Letters **106**, 190502 (2011).

[2] M. Hofmann, T. Moroder, and O. Gühne, Analytical characterization of the genuine multiparticle negativity, Journal of Physics A: Mathematical and Theoretical **47**, 155301 (2014).

[3] J. Löfberg, in *In Proceedings of the CACSD Conference* (Taipei, Taiwan, 2004).

[4] *MOSEK Optimization Toolbox for MATLAB 10.2.17*, MOSEK ApS (2024).

[5] M. Lewenstein, B. Kraus, J. I. Cirac, and P. Horodecki, Optimization of entanglement witnesses, Phys. Rev. A **62**, 052310 (2000).

[6] M. Gohlke, R. Moessner, and F. Pollmann, Dynamical and topological properties of the Kitaev model in a [111] magnetic field, Physical Review B **98**, 014418 (2018), pRB.

[7] A. Kitaev, Anyons in an exactly solved model and beyond, Annals of Physics **321**, 2 (2006).

[8] T.-A. Ohst, X.-D. Yu, O. Gühne, and H. C. Nguyen, Certifying quantum separability with adaptive polytopes, SciPost Phys. **16**, 063 (2024).

[9] E. H. Lieb, Flux Phase of the Half-Filled Band, Phys. Rev. Lett. **73**, 2158 (1994).

[10] F. Zschocke and M. Vojta, Physical states and finite-size effects in Kitaev's honeycomb model: Bond disorder, spin excitations, and NMR line shape, Phys. Rev. B **92**, 014403 (2015).

[11] H. Yao and X.-L. Qi, Entanglement Entropy and Entanglement Spectrum of the Kitaev Model, Phys. Rev. Lett. **105**, 080501 (2010).

[12] G. Baskaran, S. Mandal, and R. Shankar, Exact Results for Spin Dynamics and Fractionalization in the Kitaev Model, Phys. Rev. Lett. **98**, 247201 (2007).

[13] M. A. Levin and X.-G. Wen, String-net condensation: A physical mechanism for topological phases, Phys. Rev. B **71**, 045110 (2005).

[14] A. Hamma, R. Ionicioiu, and P. Zanardi, Bipartite entanglement and entropic boundary law in lattice spin systems, Phys. Rev. A **71**, 022315 (2005).

[15] M. Levin and X.-G. Wen, Detecting Topological Order in a Ground State Wave Function, Phys. Rev. Lett. **96**, 110405 (2006).

[16] K.-C. Ha, K. H. Han, and S.-H. Kye, Separability of multi-qubit states in terms of diagonal and anti-diagonal entries, Quantum Information Processing **18**, 34 (2018).